Single-gate tracking behavior in flat-band multilayer graphene devices

Kryštof Kolář,[1,2,*] Dacen Waters,[3,4] Joshua Folk,[5,6] Matthew Yankowitz,[3,7] and Cyprian Lewandowski[8,9]

[1]*Dahlem Center for Complex Quantum Systems and Fachbereich Physik, Freie Universität Berlin, 14195 Berlin, Germany*
[2]*Department of Applied Physics, Aalto University School of Science, FI-00076 Aalto, Finland*
[3]*Department of Physics, University of Washington, Seattle, Washington 98195, USA*
[4]*Department of Physics and Astronomy, University of Denver, Denver, Colorado 80210, USA*
[5]*Quantum Matter Institute, University of British Columbia, Vancouver, British Columbia, Canada V6T 1Z4*
[6]*Department of Physics and Astronomy, University of British Columbia, Vancouver, British Columbia, Canada V6T 1Z1*
[7]*Department of Materials Science and Engineering, University of Washington, Seattle, Washington 98195, USA*
[8]*National High Magnetic Field Laboratory, Tallahassee, Florida 32310, USA*
[9]*Department of Physics, Florida State University, Tallahassee, Florida 32306, USA*

(Received 24 March 2025; revised 3 December 2025; accepted 15 January 2026; published 13 February 2026)

A central feature of many van der Waals (vdW) materials is the ability to precisely control their charge doping, n, and electric displacement field, D, using top and bottom gates. For devices composed of only a few layers, it is commonly assumed that D causes the layer-by-layer potential to drop linearly across the structure. Here, we show that this assumption fails for a broad class of crystalline and moiré vdW structures based on Bernal- or rhombohedral-stacked multilayer graphene. We find that the electronic properties at the Fermi level are largely dictated by special layer-polarized states arising at Bernal-stacked crystal faces, which typically coexist in the same band with layer-delocalized states. We uncover a mechanism by which the layer-delocalized states completely screen the layer-polarized states from the bias applied to the remote gate. This screening mechanism leads to an unusual scenario where voltages on either gate dope the band as expected, yet the band dispersion and associated electronic properties remain primarily (and sometimes exclusively) governed by the gate closer to the layer-polarized states. Our results reveal an electronic mechanism underlying the atypical single-gate-controlled transport characteristics observed across many flat-band graphitic structures, and provide key theoretical insights essential for accurately modeling these systems.

DOI: 10.1103/j1zf-v3j5

I. INTRODUCTION

Dual-gated two-dimensional (2D) van der Waals (vdW) device structures offer unprecedented tunability, enabling simultaneous *in situ* control of the charge density and perpendicular displacement field. This capability opens a broad experimental phase space, which has driven numerous recent discoveries in various multilayer vdW systems—particularly those featuring flat electronic dispersions [1–32]. Here, we focus on a striking and nearly universal feature that has been apparent since the earliest measurements of dual-gated moiré graphene multilayers, but that has received little attention until now: the frequent appearance of diagonal lines in the filling–displacement-field (ν-D) plane.

An example of such behavior is shown in Fig. 1(a) for twisted double bilayer graphene (TDBG), where diagonal features tracking a single-gate voltage have been observed in dozens of devices [25–30]. The figure shows a longitudinal resistance (R_{xx}) map in the ν-D plane for one such TDBG device, with arrows highlighting directions of constant bottom (n_b) and top (n_t) gate charge density (proportional to V_b and V_t). Two key observations are a set of resistive bumps forming a crosslike feature for hole-type doping ($\nu < 0$) centered at $D = 0$, and a high-resistance region associated with broken spin and valley degeneracies for electron-type doping ($\nu > 0$) at larger $|D|$. The crosslike feature is approximately aligned with axes of constant n_b or n_t, as is the boundary of the symmetry-breaking region.

The association of spin and valley symmetry breaking, hereafter referred to as flavor symmetry breaking, with a single-gate voltage is even more evident in the transverse resistance (R_{xy}) map of Fig. 1(b), corresponding to a twisted bilayer-trilayer graphene device. The abrupt sign change in R_{xy} appearing at $V_b = -4.9$ V corresponds to a transition from an unpolarized metallic phase to a metallic phase with full isospin degeneracy breaking. The symmetry-breaking transition is completely decoupled from V_t over a wide voltage range. In contrast, other features of the maps in Figs. 1(a) and 1(b)—such as band insulators and correlated insulators at integer ν—exhibit no gate-tracking effect, remaining vertical in the ν-D plane and thus pinned to fixed ν. In this context, the gate-tracking behavior is striking: it challenges the usual assumption that D and ν alone define the boundaries of characteristic regions in experimental phase diagrams, suggesting instead that a single-gate voltage can play a decisive role.

The 2D vdW materials that exhibit this gate-tracking behavior most prominently are TDBG [25–27,29,30], related

*Contact author: kolar@zedat.fu-berlin.de

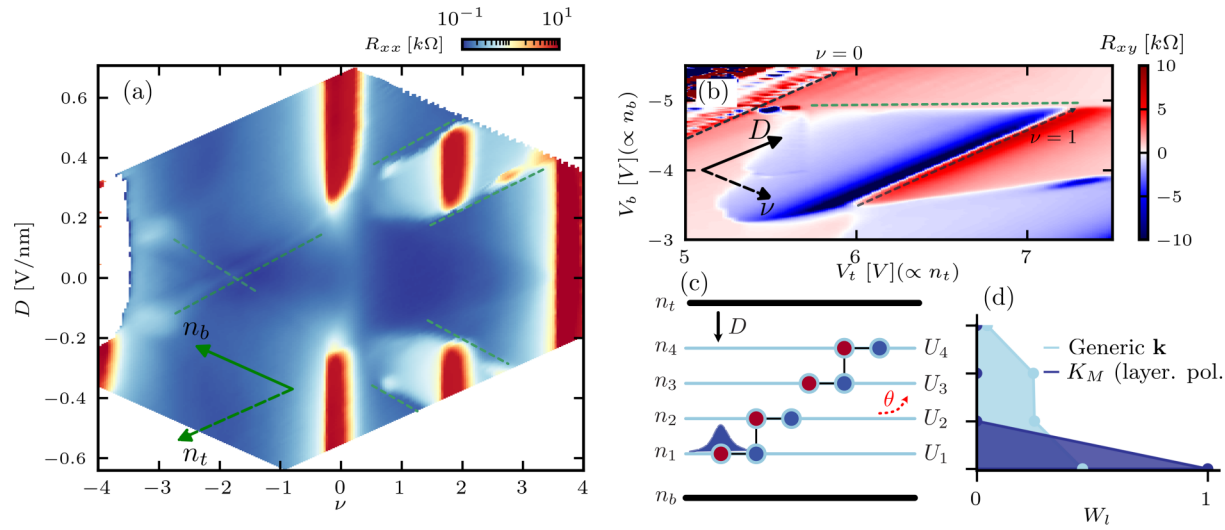

FIG. 1. (a) Experimental R_{xx} map of twisted double bilayer graphene with twist angle $\theta = 1.30°$. The bottom and top gate axes are indicated by the green arrows. The onset of symmetry breaking at $\nu > 0$ is tuned by n_b for $D > 0$ and n_t for $D < 0$. The data are from Ref. [29]. Features closely tracking a single gate are highlighted with green dashed lines. (b) Experimental R_{xy} map of twisted bilayer-trilayer graphene with twist angle $\theta = 1.50°$ as a function of the top (V_t) and bottom (V_b) gate voltages. Insulators at $\nu = 0$ and 1 appear diagonally in this plot, and are highlighted using black dashed lines. The horizontal dashed green line denotes a transition between a normal metal and a quarter-metal phase. The data are from Ref. [28]. (c) Schematic of a doubly gated Bernal-terminated device, illustrating the bottom layer sublattice-polarized surface state in blue. The blue lines denote graphene layers, and the black lines denote the top and bottom gate surfaces. (d) Relative layer occupations W_l for the layer-polarized state at K_M (dark blue), and those of some generic bulk state (light blue). Note the perfect polarization of the layer-polarized state to the bottom layer.

structures with different numbers of twisted graphene layers [28,32,33], and rhombohedral graphene aligned with hexagonal boron nitride [22–24]. A key microscopic feature of these graphene-based systems is the presence of robust layer- and sublattice-polarized states at the K and K' points of the monolayer Brillouin zone, arising from the local AB (Bernal) stacking arrangement between neighboring graphene sheets away from any twisted interface. The schematic in Fig. 1(c) shows the case of TDBG, formed by twisting two Bernal bilayers. In this system, there is a layer-polarized state in the two outermost layers, but in other multilayer graphene systems the relevant layer-polarized state may be internal [28] (see Supplemental Material [34] for a detailed discussion). The bottom layer-polarized state is relevant for $D > 0$, making up a layer-polarized "pocket" that coexists with more delocalized states within a single band [Fig. 1(d)]. The gate-tracking behavior then generally arises from a combination of two effects: (i) the layer-polarized pocket [on layer 1 in Fig. 1(c)] predominantly controls the onset of symmetry-breaking phases due to its high density of states (DOS), and (ii) the delocalized states screen the layer-polarized pocket from the potential applied to the remote gate [the top gate in Fig. 1(c)]. The interplay of these two effects naturally leads to single-gate tracking of the symmetry-breaking boundary, as seen in Figs. 1(a) and 1(b).

In this paper, we analyze the gate-tracking mechanism to delineate its microscopic origins, examine its ubiquity in moiré graphene structures, and assess its robustness. We begin by clarifying the pivotal role of layer-polarized states in shaping the band structure of Bernal-terminated multilayer systems. Then, we introduce a simple electrostatic model that provides an analytical view of how the layer-polarized states evolve in the ν-D plane, revealing a mechanism by which the delocalized states screen the layer-polarized states. Finally, we apply this framework to TDBG, performing numerical mean-field simulations that may then be compared to experiment observations, for example in Fig. 1(a). Our calculations employ a microscopically accurate model of TDBG that incorporates the role of moiré potential. The self-consistent mean-field simulations include Fock-driven symmetry breaking in addition to Hartree electrostatics. Although we focus on TDBG for clarity, our theory establishes a general mechanism that applies to any multilayer systems with Bernal stacking as a component of its structure, including rhombohedral multilayer graphene and twisted bilayer-trilayer graphene. Appropriately generalized, our theory should also apply to any layered system featuring perfectly polarized states, such as twisted bilayer transition-metal dichalcogenides.

II. RESULTS

A. Systems with a Bernal-stacked interface: Perfectly layer-polarized states near the *K* point

We begin by reviewing the properties of 2D graphene multilayer systems that feature a Bernal-stacked interface. Although our discussion focuses on a bottom Bernal termination, the same ideas extend to bands residing primarily on internal Bernal-stacked interfaces (see Supplemental Material [34]). Labeling the atomic orbitals in the two terminating Bernal layers as $A1$, $B1$, $A2$, and $B2$—where A/B denotes sublattices and $l = 1, 2$ labels the layers—local Bernal stacking implies that only the $B1 \to A2$ interlayer tunneling is significant. This arrangement yields a state at the K point that is fully polarized to the bottom layer, even when other states away from the K point are not bound to the surface.

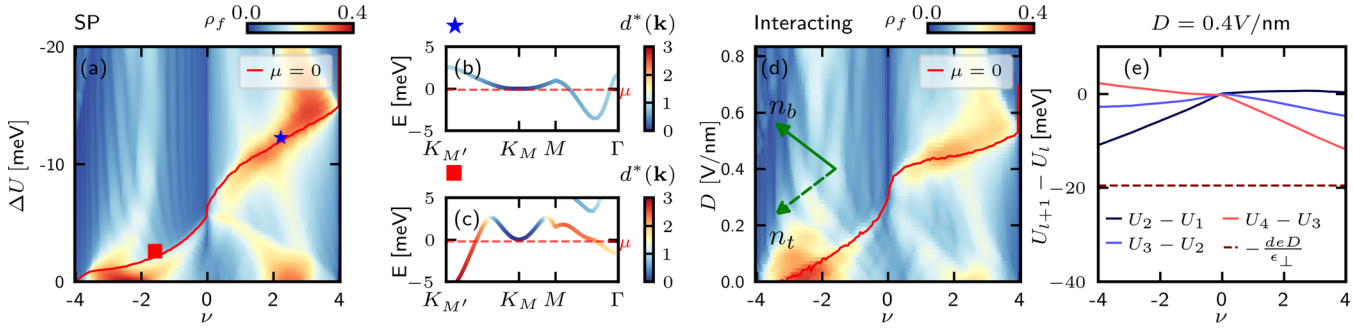

FIG. 2. (a) Single-particle (SP) ΔU vs ν map of the density of states per flavor, ρ_f. Here the difference ΔU is identical between all layers. The contour of the layer-polarized states from the Bernal stacking termination ($\mu = 0$) is shown in orange. (b) Single-particle band structure at $\nu > 0$ at the position of the blue star in (a). The color code shows the average distance of the state $d^*(\mathbf{k})$ from the bottom-most layer. The bottom layer layer-polarized states have $d^*(K_M) = 0$. (c) Same as (b), but at the position of the red square of (a). (d) Numerical ν-D color map of the density of states per flavor (ρ_f) together with the line of $\mu = 0$ meV. We work in the Hartree approximation with dielectric constant $\varepsilon_\perp = \varepsilon_\parallel = 6$ (see Supplemental Material [34] for details and further discussion about possible $\varepsilon_\parallel$ and $\varepsilon_\perp$ dependence). (e) $U_{l+1} - U_l$ as a function of ν at $D = 0.4$ V/nm within the self-consistent Hartree calculation [obtained from Eq. (5)], compared to the naive value $-deD/\varepsilon_\perp$.

In the basis $\Psi_{\mathbf{k}} = (c_{\mathbf{k},A1}, c_{\mathbf{k},B1}, c_{\mathbf{k},A2}, c_{\mathbf{k},B2}, \dots)$, the single-particle Hamiltonian near the K point, for a device with Bernal stacking on the first two layers, takes the form [35–37]

$$H_{\mathrm{kin}} + H_\perp = \sum_{\mathbf{k}} \Psi^\dagger_{\mathbf{k}} \begin{pmatrix} U_1 & v_F\bar{k} & -v_4\bar{k} & -v_3 k & 0 \\ v_F k & U_1 & t_1 & -v_4\bar{k} & \\ -v_4 k & t_1 & U_2 & v_F\bar{k} & \\ -v_3\bar{k} & -v_4 k & v_F k & U_2 & \\ 0 & & & & \ddots \\ \vdots & & & & \end{pmatrix} \Psi_{\mathbf{k}}, \tag{1}$$

where $k = k_x + ik_y$ and $\bar{k} = k_x - ik_y$ momenta are measured from the K point, v_F is the graphene Dirac velocity, $v_3, v_4 \ll v_F$ denote nonlocal interlayer tunneling velocities, and t_1 is the strength of $B1 \to A2$ tunneling. A key ingredient in the above Hamiltonian is the layer-dependent electrostatic potential U_l [depicted in Fig. 1(c); l denotes the layer index]. In the next section, we derive how U_l depends on charges on the top (n_t) and bottom (n_b) gates. Note that for clarity here we do not explicitly list all entries of the full moiré Hamiltonian—in particular, we omit the moiré potential originating from the twisted interface. We do however include the moiré potential in all of our calculations, and in the Supplemental Material [34] we explicitly discuss its details.

The layer-polarized state on the $A1$ orbital is an exact layer and sublattice polarized eigenstate of Eq. (1) at the K point ($\mathbf{k} = 0$) with energy U_1 and is also spin and valley degenerate. For small $\mathbf{k}$ away from the K point, states retain strong layer polarization, forming a well-defined pocket of layer-polarized states. The peculiarity of moiré systems featuring Bernal interfaces that distinguishes them from standard Bernal bilayer graphene is that this pocket exists within a well-defined flat moiré band. As we will show, this high density-of-states pocket controls symmetry breaking, and responds primarily to the proximal gate as a result of its layer polarization. For simplicity, throughout the remainder of the paper we measure energies with respect to U_1, effectively defining $U_1 = 0$. In this convention, the layer-polarized state is at the Fermi level when the chemical potential is zero ($\mu = 0$).

To illustrate the role of the layer-polarized pocket, we now examine its impact on the band structure of TDBG, where we consider a twist angle of $\theta = 1.3^\circ$ at which the moiré potential optimally flattens the conduction band. Figure 2(a) shows a map of the single-particle DOS calculated as a function of the filling factor ν and an interlayer potential difference $\Delta U = U_{l+1} - U_l$ (see Supplemental Material [34] for full details of the model). Here, ν and ΔU are treated as theoretical parameters; later, we will connect them to experimentally tunable gate charges. A prominent feature in Fig. 2(a) is a region of enhanced DOS associated with a flat part of the band at positive ν. Overlaying the $\mu = 0$ contour reveals that this high-DOS region coincides with the layer-polarized state being exactly at the Fermi level. A similar high DOS feature also appears for negative filling, although it aligns less precisely with the $\mu = 0$ condition.

The interpretation of the layer-polarized pocket as the source of the high density of states is confirmed by considering the band structures at specific points along the $\mu = 0$ contour, shown in Figs. 2(b) and 2(c), where we color code each state in the band by its average distance from the bottom layer, $d^*(\mathbf{k}) \equiv \sum_l (l-1) W_l(\mathbf{k})$, where $W_l(\mathbf{k})$ is the layer distribution. The pocket is centered around the K point of the lower bilayer, K_M. For $\nu > 0$ [Fig. 2(b)] the entire band (not just the pocket) is strongly polarized to the bottom of the structure, resulting in a quenching of the layer-polarized pocket dispersion. Figure 2(c) shows the contrasting case of $\nu < 0$, in which most of the moiré band is widely distributed across the layers leading to a larger dispersion of the layer-polarized pocket. In what follows, we employ the zero-energy layer-polarized state (at $U_1 = 0$) as a theoretical reference point, serving to clarify how the layer-polarized pocket evolves with gating in the band structure and explaining the experimental single-gate tracking.

B. Relating layer potentials to the gate charges

We now develop a framework for properly describing the electrostatics of multilayer devices, which is crucial for

understanding the band structure evolution with density ν and displacement field D (rather than the interlayer potential difference ΔU). Consider a multilayer system with N layers labeled $l = 1, \ldots, N$, sandwiched between the bottom and top gates, as shown in Fig. 1(c). We denote the net electron densities in each layer l by n_l, and in the top and bottom gates by n_t and n_b, respectively. Ignoring quantum capacitance effects (as is valid when the gate–sample capacitance is small), these densities relate to the top and bottom gate voltages as $n_t = -\frac{1}{e}C_{tg}V_t$ and $n_b = -\frac{1}{e}C_{bg}V_b$, where C_{tg} and C_{bg} are the top and bottom gate capacitances per unit area, and e is the electron charge. Overall charge neutrality implies that the sum of these gate charges fixes the total device density, $n = \sum_l n_l = -(n_t + n_b)$. We note that we are working in terms of gate charges throughout as they are the more convenient variables when considering screening of electric fields as opposed to gate potentials. Their difference sets the experimentally accessible displacement field, $D = e\frac{n_b - n_t}{2\varepsilon_0} = \frac{C_{tg}V_t - C_{bg}V_b}{2\varepsilon_0}$. The full Hamiltonian is thus

$$\widehat{\mathbf{H}} = H_{\text{kin}} + H_{\text{int},\mathbf{q}\neq 0} + H_{\perp}, \tag{2}$$

where H_{kin} is the single-particle Hamiltonian at zero out-of-plane electric field ($U_l = 0$), $H_{\text{int},\mathbf{q}\neq 0}$ is the finite-momentum density-density Coulomb interaction (excluding its uniform, multilayer component), and $H_{\perp}$ is the uniform, multilayer part of the Coulomb interaction originating from out-of-plane electric fields [37–41]:

$$H_{\perp} = \sum_{l=1}^{N} U_l \, \mathcal{P}_l \tag{3}$$

where $\mathcal{P}_l$ is the projector onto layer l, and U_l are the self-consistent layer potentials. To find U_l, we integrate Gauss's law across the layers:

$$U_{l+1} - U_l = -e^2 d \frac{n_b + \sum_{j\leqslant l} n_j}{\varepsilon_{\perp}\varepsilon_0}, \tag{4}$$

with d the interlayer distance and $\varepsilon_{\perp}$ the out-of-plane dielectric constant. Together, $H_{\text{kin}} + H_{\perp}$ form the single-particle description of Eq. (1), with U_l subject to the recursion relation of Eq. (4) [42].

This formulation treats out-of-plane electric fields due to charges in the gates and in the sample on the same footing, in keeping with Gauss's law. The practice of incorporating an unscreened displacement field $D = e\frac{n_b - n_t}{2\varepsilon_0}$ in the microscopic Hamiltonian of Eq. (1) as a constant potential difference $\Delta U = -deD/\varepsilon_{\perp}$ between layers, as is typically done in single-particle approaches, is generally not correct. This is best seen by rewriting the potential difference from Eq. (4) explicitly in terms of D:

$$U_{l+1} - U_l = -\frac{deD}{\varepsilon_{\perp}} + \frac{e^2 d}{2\varepsilon_{\perp}\varepsilon_0}\left[n - 2\sum_{j\leqslant l} n_j\right]. \tag{5}$$

The second term, present even at zero displacement field, is necessary to comply with Gauss's law. Already at zero doping ($n = 0$), this term enables screening of the displacement field by the system [37,39,40]. For nonzero doping, it also includes the additional electric field from the gates due to doping [38]. Capturing both effects is crucial for an accurate analysis in the ν-D plane.

To illustrate the merits of this framework, Fig. 2(d) shows the self-consistently determined Hartree DOS, along with the contour of $\mu = 0$ (e.g., the layer-polarized state energy). Note that here we treat the finite-$\mathbf{q}$ interaction within the Hartree approximation, neglecting exchange effects and ignoring the possibility of isospin symmetry breaking. Importantly, in contrast with Fig. 2(a), the vertical axis here is D. Using Gauss's law then allows us to also plot the gate density (n_t, n_b) axes in green. We further note that our method avoids bias by using the same plane wave basis set for different values of D and ν (see Supplemental Material [34]).

A key observation is that, for $\nu < 0$, the layer-polarized state $\mu = 0$ contour aligns with the n_t axis (constant n_b). We will show in the following section that this layer-polarized state behavior arises due to the large spatial separation between the layer-polarized state in the bottom layer and the rest of the highest moiré valence band, which is situated towards the center of the TDBG structure [see Fig. 2(c)] and efficiently screens the top gate. For $\nu > 0$, the layer-polarized state contour is significantly more horizontal than the n_t axis, which we will show results from overscreening. Upon developing a physical understanding of the layer-polarized state behavior in the two-gate geometry, we will show later that when symmetry breaking is included, the system recovers the experimentally seen single-gate tracking even at $\nu > 0$.

To further illustrate the importance of determining the layer potentials correctly, in Fig. 2(e) we show $U_{l+1} - U_l$ within the self-consistent Hartree calculation compared to the "conventional" result of $U_{l+1} - U_l = -\frac{deD}{\varepsilon_{\perp}}$. In the conventional approach, i.e., keeping only the first term in Eq. (5), the potentials do not depend on ν, unlike the self-consistent solution, i.e., keeping all terms in Eq. (5), which strongly depends on ν. Crucially, the true potentials deviate from the conventional result not only in magnitude, but also in the sign of the energy difference, suggesting a possibility for nontrivial state renormalization with external displacement field. Lastly, in Supplemental Material Fig. S1 we show the expected $\mu = 0$ contours computed using the self-consistent framework and the conventional approach for several dielectric constants $\varepsilon_{\perp}$. This comparison highlights that only with layer potentials single-gate tracking occurs generically (for $\nu < 0$) for a wide range of dielectric constants. A calculation using conventional relation $U_{l+1} - U_l$ with D would only yield single-gate tracking for a limited doping range if the dielectric constant is fine tuned.

C. Physical origins of the gate tracking behavior

We now develop a qualitative understanding of the screening mechanisms at play in determining the evolution of the layer-polarized state (or equivalently the $\mu = 0$ contour) in the ν-D plane, using an analytical model that includes the effects of both H_{kin} and $H_{\perp}$ in Eq. (2). We first write down the compressibilities relative to the top and bottom gates, $\frac{\partial\mu}{\partial n_t}$ and $\frac{\partial\mu}{\partial n_b}$, given by

$$\frac{\partial\mu}{\partial n_t} = \frac{\partial\mu}{\partial n}\frac{\partial n}{\partial n_t} + \sum_l W_l \frac{\partial U_l}{\partial n_t}, \tag{6}$$

$$\frac{\partial\mu}{\partial n_b} = \frac{\partial\mu}{\partial n}\frac{\partial n}{\partial n_b} + \sum_l W_l \frac{\partial U_l}{\partial n_b} \tag{7}$$

where $W_l = \partial\mu/\partial U_l$ denotes the fraction of electronic states in layer l at the Fermi level ($\sum_l W_l = 1$) [43].

Due to the explicit presence of the n_b term in Eq. (4), the potentials U_l respond differently to the two gates (see Supplemental Material [34] for derivation). This leads to

$$-\frac{\partial\mu}{\partial n_b} = \frac{1}{\rho} - \frac{e^2\Delta d}{\tilde{\varepsilon}_\perp\varepsilon_0} + \frac{e^2 d^*}{\tilde{\varepsilon}_\perp\varepsilon_0}, \tag{8}$$

$$-\frac{\partial\mu}{\partial n_t} = \frac{1}{\rho} - \frac{e^2\Delta d}{\tilde{\varepsilon}_\perp\varepsilon_0} \tag{9}$$

where we relate $\partial\mu/\partial n$ with the inverse density of states, $1/\rho$, at the Fermi level, and use an effective dielectric constant $\tilde{\varepsilon}_\perp > \varepsilon_\perp$ to account for additional screening by bands away from the Fermi level. We have also introduced two effective parameters, d^* and Δd, defined via

$$d^* = d\sum_{l=1}^{N}(l-1)W_l, \tag{10}$$

$$\Delta d = \frac{d}{2}\sum_{l,l'=1}^{N}|l'-l|W_l W_{l'}, \tag{11}$$

which capture, respectively, the average distance of the charges at the Fermi level from the bottom-most ($l = 1$) layer and their average vertical spread across the layers, as illustrated in Fig. 3(a). Note that $d^* \geqslant \Delta d$, and both ρ and W_l generally depend on the instantaneous gate configurations. We note in passing that the asymmetry of Eqs. (8) and (9) stems from the choice of the convention $U_1 = 0$.

These expressions can be understood as follows. In addition to the standard compressibility $\frac{1}{\rho}$, the states at the Fermi level experience electrostatic shifts due to changes in the layer potentials U_l as the gate charges vary. Both gates induce the same change in the layer distribution, δn_l, yielding a self-interaction term proportional to Δd. Meanwhile, the bottom gate adds an extra shift proportional to d^*, the average distance from the bottom layer. This asymmetry arises due to the explicit n_b term in Eq. (4), which comes from the gauge choice $U_1 = 0$, pinning the layer-polarized state energy to μ alone [see discussion below Eq. (1)]. In a different gauge, the relevant quantity for the layer-polarized state would be $\mu - U_1$, but the same physical conclusions would follow.

Next, we relate the gate-projected compressibilities ($\frac{\partial\mu}{\partial n_{b/t}}$) in Eq. (9) to the experimentally observed layer-polarized state trajectory in the n_b, n_t plane. For small changes in gate charges, the chemical potential changes as

$$\mathrm{d}\mu = \frac{\partial\mu}{\partial n_b}\delta n_b + \frac{\partial\mu}{\partial n_t}\delta n_t, \tag{12}$$

where $\delta n_{t/b}$ are small increments in the top/bottom gate densities. Constant-μ trajectories thus satisfy

$$\delta n_b = -\alpha\delta n_t, \tag{13}$$

where we introduce

$$\alpha \equiv \frac{\partial\mu}{\partial n_t}\Big/\frac{\partial\mu}{\partial n_b} = \frac{1-\frac{e^2\Delta d}{\tilde{\varepsilon}_\perp\varepsilon_0}\rho}{1+\left(\frac{d^*}{\Delta d}-1\right)\frac{e^2\Delta d}{\tilde{\varepsilon}_\perp\varepsilon_0}\rho}, \tag{14}$$

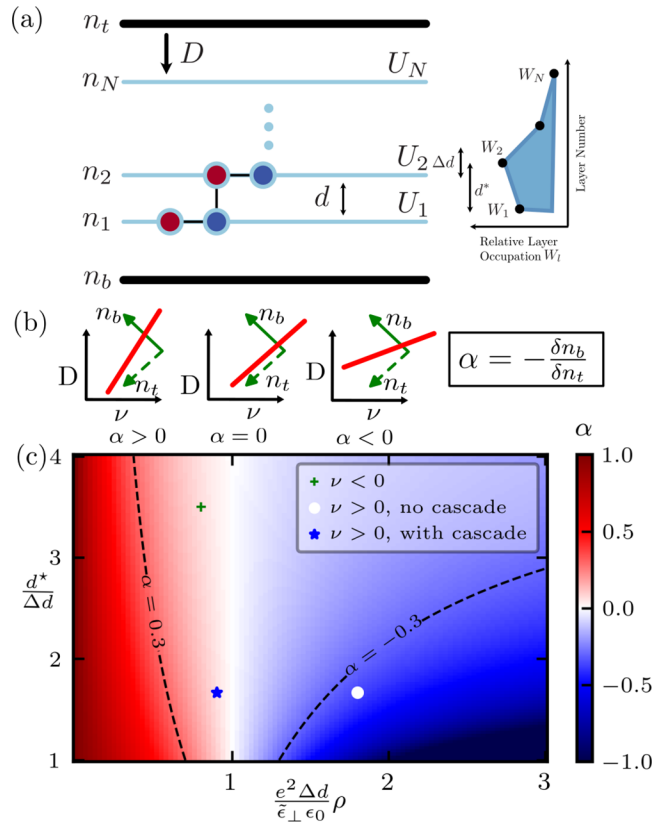

FIG. 3. (a) Sketch of the theoretical setup, showing the gates and the layered material. We assume the bottom two layers have Bernal (*AB*) stacking, leading to layer-polarized states at the bottom-most surface. The average distance of carriers from the bottom layer d^* and the average vertical spread Δd are shown. (b) Schematic illustration of the behaviors expected for different values of α. (c) Map of α [Eq. (14)] as a function of $d^*/\Delta d$ and $\frac{e^2\Delta d}{\varepsilon_\perp\tilde{\varepsilon}_0}\rho$. $\alpha = 0$ corresponds to perfect gate tracking. Contours of $|\alpha| = 0.3$ are shown in dashed black. Estimated parameter values for TDBG at $\nu < 0$ and $\nu > 0$ without and with flavor symmetry breaking (cascade) are also shown.

as the ratio of the two gate-projected compressibilities defined in Eq. (9). The parameter α is directly connected to screening of the layer-polarized pocket from the top gate potential, setting the slope of the constant-μ contours as sketched schematically in Fig. 3(b). $\alpha \to 0$ corresponds to perfect screening: the $\mu = 0$ contour runs parallel to the n_t axis, implying that the layer-polarized state is tuned only by the bottom gate. For $\alpha > 0$, the contour tilts toward the D axis. The layer-polarized pocket is underscreened from the top gate, and at $\alpha = 1$ it is tuned equally by both gates following the naive picture often applied to 2D stacks. For $\alpha < 0$, the contour tilts towards the ν axis, corresponding to overscreening.

We note at this point that in Eq. (14), the parameters should be mathematically understood to correspond to the screening (delocalized) states only and excluding the contribution of the layer-polarized pocket. We derive this result rigorously in the Supplemental Material [34], but summarize here that physically it results from the fact that for the single-gate tracking mechanism to occur, two types of states are required: (i) those localized at one of the surfaces and (ii) a delocalized high-DOS state in the bulk of the device. Here, the state (i) is

the layer-polarized state, the occupation of which is constant along the $\mu = 0$ contour, and it does not contribute to screening; only the states (ii) do by screening the gate remote to the layer-polarized state, and hence they enter into the effective parameters of Eq. (14).

To gain further insight, we plot α as a function of the dimensionless parameters $\frac{d^*}{\Delta d} \geqslant 1$ and $\frac{e^2 \Delta d}{\tilde{\varepsilon}_\perp \varepsilon_0}\rho$ in Fig. 3(c). $\frac{d^*}{\Delta d}$ reflects the degree to which the layer-polarized and delocalized states can be thought of as independent conducting sheets, whereas $\frac{e^2 \Delta d}{\tilde{\varepsilon}_\perp \varepsilon_0}\rho$ reflects the strength of out-of-plane Coulomb self-interactions with respect to kinetic energy. When there are no screening states, $\rho = 0$ so $\alpha = 1$, and μ depends only on filling ν. Increasing the number of screening states, ρ, causes α to decrease until

$$\frac{e^2 \Delta d}{\tilde{\varepsilon}_\perp \varepsilon_0}\rho = 1, \tag{15}$$

at which point $\alpha = 0$ and the top gate is completely screened ($\frac{\partial \mu}{\partial n_t} = 0$). For even larger ρ, $\alpha < 0$, which corresponds to overscreening. Increasing the ratio $\frac{d^*}{\Delta d}$ serves to broaden the regime of $|\alpha| \ll 1$ [see, for example, the dashed curve corresponding to $|\alpha| = 0.3$ in Fig. 3(c)]. This corresponds to a situation in which the delocalized states have a larger vertical separation from the layer-polarized states, and can thus screen the adjacent gate more effectively.

We now comment on three relevant theoretical extensions of this model, all of which act to increase α, i.e., move system parameters effectively to the left in Fig. 3(c). First, the in-plane Hartree correction [coming from the $H_{\text{int},\mathbf{q}\neq 0}$ terms in Eq. (2)] renormalizes the band structure. However, the layer-polarized state of Eq. (1) has zero in-plane inhomogeneity, and is not (to first order) affected by in-plane Hartree. As a result, the nonsurface states will shift upward with respect to the layer-polarized state, reducing the effective value of ρ and increasing α. Second, if the states of interest in the layer-polarized pocket have some finite weight on the second layer W_2^{lp}, then they are at the Fermi level when $\mu - W_2^{lp} U_2 = 0$. We show in the Supplemental Material [34] that this effect also increases α. Third, due to its strong layer localization, we expect exchange effects to be stronger within the layer-polarized pocket than within the rest of the band. Effectively, upon doping, the screening states shift upward relative to the layer-polarized pocket, decreasing the effective ρ, and increasing α.

We conclude this section by highlighting a subtle and surprising implication of Eq. (15), which is that single-gate tracking can occur even in few-layered systems. The microscopic origin is the vertical delocalization ($\Delta d \neq 0$) of the screening states. An intriguing feature of this mechanism is that it allows overscreening ($\alpha < 0$) to occur. Interestingly, for fixed Δd and d^*, the infinite density-of-states limit ($\rho \to \infty$) always leads to some overscreening, as we have

$$\lim_{\rho \to \infty} \alpha = -\frac{\Delta d}{d^* - \Delta d} < 0. \tag{16}$$

However, for large $d^*/\Delta d$, $\alpha \approx 0$ and perfect gate tracking is recovered. Thus, starting from a system with $\alpha \to \infty$, where features only follow filling ν (such as few layer graphene), the additional presence of delocalized screening states improves single-gate tracking, i.e., moves to the right of Fig. 3(c), even in the imperfect $d^* \approx \Delta d$ regime. However, single-gate tracking becomes ideal when $d^* \gg \Delta d$, moving up in Fig. 3(c). The regime of large $d^*/\Delta d$ is naturally realized in semimetallic rhombohedral graphene [44–48]. This systems exhibits a high density of states that is localized to the outermost surface layers of the crystal, such that $d^*/\Delta d \gg 1$, implying $\alpha \approx 0$ in Eq. (16).

D. Relation to experimental observations

We now apply the above mechanism to real systems and connect to experimental observations. First, consider TDBG at $\nu < 0$, where we found that the layer-polarized state in Fig. 2(d) was primarily tuned by a single gate. In this regime of TDBG, $d^* \approx 2d$, while $\Delta d \approx 0.6d$, since the screening states [see Fig. 2(c)] are concentrated near the other end of the stack. Figure 3(c) then predicts a robust large region of small $|\alpha|$ in parameter space, which we confirm in the Supplemental Material [34], finding the slope of the $\mu = 0$ contour to be largely independent of the dielectric constant $\varepsilon_\perp$. Coming back to the experimental result in Fig. 1(a), we interpret the gate-tracking crosslike features for $\nu < 0$ as corresponding to the disappearance of the layer-polarized pocket, as, qualitatively, local high resistance regions can be associated with regions of high density of states.

Next, we consider the gate tracking of symmetry-breaking boundaries occurring at $\nu > 0$. Although the precise value of α varies between systems, it appears to be an experimental fact that $\alpha > 0$ for most symmetry-breaking phase boundaries. On the other hand, in TDBG in the flavor-degenerate calculation of Fig. 2(d), the layer-polarized state is overscreened ($\alpha < 0$), a behavior enabled by the delocalization of the screening states. However, since the $\mu = 0$ contour is associated with a high density of states, we expect the system, according to the Stoner criterion [49], to be unstable towards symmetry breaking, reducing the density of states. Provided that phase transitions are triggered when the layer-polarized state crosses the Fermi level within the symmetry-broken phase, the evolution of the phase boundary in the ν-D plane follows from our present framework. Crucially, reduction of the density of states effectively moves the system parameters towards the left of Fig. 3(c), increasing the value of α. At $\nu > 0$, TDBG has $d^* \approx d$ and $\Delta d \approx 0.6d$ as numerically estimated from the model in Sec. II A. A back of the envelope calculation, estimating $\rho \approx 0.1 N_f / A_{\text{UC}}\ (\text{meV})^{-1}$, where N_f is the number of active flavors and A_{UC} is the moiré unit cell area, gives $\frac{e^2 \Delta d}{\tilde{\varepsilon}_\perp \varepsilon_0}\rho \approx 0.44 N_f$ for $\tilde{\varepsilon}_\perp \approx 8$. In an unpolarized phase, $N_f = 4$, predicting overscreening with $\alpha < 0$. If instead symmetry breaking occurred (i.e., a half-metal phase with $N_f = 2$) a small positive α would be obtained, as depicted in Fig. 3(c).

We now show that the layer-polarized state is indeed relevant for symmetry-breaking transitions. To that end, we adopt a minimal mean-field model of flavor symmetry breaking [50], which shifts each flavor by an amount proportional to its filling:

$$H_{\text{Fock}} = -U_{\text{Fock}} \text{Diag}(\nu_{K\uparrow}, \nu_{K'\uparrow}, \nu_{K'\downarrow}, \nu_{K\downarrow}), \tag{17}$$

where ν_f is the filling of flavor f relative to charge neutrality, and U_{Fock} sets the interaction strength. For simplicity, we only

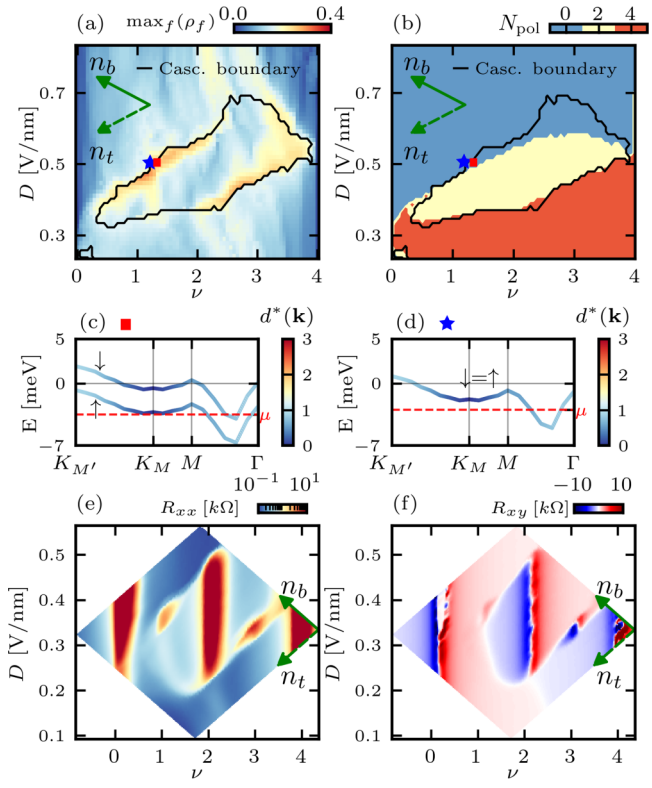

FIG. 4. (a) Density of states for the dominant flavor for $U_{\rm Fock} = 5.9$ meV and $\varepsilon_\perp = \varepsilon_\parallel = 6$, with the boundary of cascade (symmetry-breaking) region highlighted. (b) Same as (a) but for layer-polarized state occupation $N_{\rm pol}$. (c) Spin-resolved band structures at the red square point of (a), inside the symmetry-broken region. (d) Spin-resolved band structures at the blue star point of (a), just outside the symmetry-breaking region. Note the bands are spin degenerate. (e) Experimental R_{xx} map of twisted double bilayer graphene, zoomed in to the symmetry-breaking region. The data are from Ref. [29]. (f) Same as (e) but for R_{xy}.

consider valley-degenerate symmetry breaking by imposing $\nu_{K'\uparrow} = \nu_{K\uparrow}$ and $\nu_{K'\downarrow} = \nu_{K\downarrow}$—meaning the only competing phases at noninteger fillings are a spin-polarized half metal, and metal with unbroken flavor symmetry.

By optimizing the charge distribution between the two spins for different values of ν and D, we obtain the phase diagram shown in Fig. 4(a) (see Supplemental Material [34] for details of the calculation). The boundary of the symmetry-broken region, shown with a black line in Fig. 4(a), is marked by a sharp drop in the density of states. Furthermore, close to the symmetry-breaking boundaries, the layer-polarized state occupation $N_{\rm pol}$ (i.e., how many of the four spin/valley layer-polarized $\mathbf{k} = 0$ states are occupied) changes nearly simultaneously [as shown in Fig. 4(b)]. These plots support an interpretation of the transition from the half-metal phase into the symmetry-unbroken state as arising from the depletion of the layer-polarized pocket, which has high density of states. This interpretation is further confirmed by inspecting the band structures close to the transition point, shown in Figs. 4(c) and 4(d) . In the polarized (half-metal) phase [Fig. 4(c)], the high density-of-states surface pocket is emptied just before the transition. This emptying of the surface pocket renders the polarized state energetically unfavorable, triggering a transition into the unpolarized state [Fig. 4(d)]. The slope of the transition line is thus set by the slope of the layer-polarized pocket within the symmetry-broken phase. This calculation captures the experimental observations from Fig. 1(a), along with the high-resolution zoom-in maps from the TDBG device, which we show in Figs. 4(e) and 4(f). The present pocket-depletion mechanism applies for transitions from a polarized into a symmetry-unbroken phase, such as the half-metal to metal transition in TDBG [Fig. 4(f)], and the quarter-metal to metal transition in twisted bilayer-trilayer graphene [Fig. 1(b)].

As mentioned above, α is typically positive, but varies from system to system and as a function of twist angle. For example, the half-metal to metal transition in twisted monolayer-bilayer graphene [28,33] has a larger α than for TDBG [Fig. 4(f)]. Within our framework, this would naturally occur because of a smaller delocalization and/or density of states of the screening states. On the other hand, in twisted bilayer-trilayer graphene, the transition from the quarter-metal exhibits perfect gate tracking [Fig. 1(b)], which would imply higher density of states than TDBG. This conclusion is further supported by the observation of spontaneous electronic crystallization behavior at $\nu = 1/4$ [32]. Lastly, we comment on the apparent lack of experimental manifestation of features with $\alpha < 0$ slope. The layer dependent Coulomb interaction [38] in the Fock term, as well as the effect of finite delocalization of the layer-polarized pocket, would act to increase the value of α, making experimental observation of $\alpha < 0$ less likely, but still possible in principle.

III. DISCUSSION

Motivated by unexplained experimental trends, we have identified a largely overlooked element of theoretical modeling in both crystalline and moiré graphene multilayer structures: the self-consistently determined layer potentials. Our findings broadly apply to systems with flat electronic bands and a Bernal-stacked interface. By analyzing the microscopic Hamiltonian, we showed that perfectly layer-polarized states due to Bernal-stacked interfaces appear as a pocket in momentum space, forming a portion of a larger moiré band. We further showed that this pocket is responsible for symmetry-breaking transitions and other features in the ν-D plane. Exploiting its perfect layer polarization, we constructed an analytic framework based on accurate electrostatics to derive necessary criteria for the single-gate tracking of the layer-polarized pocket, uncovering a mechanism by which it is screened from a remote gate and offering a unified perspective on experimentally observed diagonal features in various vdW systems. We supported our analytical findings with mean-field calculations, determining layer potentials self-consistently, thereby reproducing experimental trends.

Our analysis focused on cases where the bottom-layer surface states dominate, corresponding to positive displacement fields that favor conduction electrons in the lower graphene layers. By symmetry, the same physics applies to the upper surface for negative displacement fields. Although we concentrated on twisted double-bilayer graphene, our framework can be extended to other multilayer graphene systems with local Bernal stacking, such as twisted bilayer-trilayer

graphene, and rhombohedral multilayers ranging from thin films to bulk flakes. In particular, rhombohedral pentalayer graphene demonstrates a tendency towards single-gate tracking at small positive filling factors (e.g., Refs. [22–24]), occasionally coinciding in the ν-D plane with a region exhibiting robust correlations and quantum anomalous Hall states. The coexistence of the two effects potentially hints at a connection between strong correlations and single-gate tracking. Recently, several experimental papers have reported single-gate tracking behavior in multilayer rhombohedral graphene [45–48], arising when valence and conduction bands with high density of states simultaneously cross the Fermi surface. Crucially, states from each band are polarized to opposite crystal surfaces. Such a configuration is naturally expected to give rise to a single-gate tracking through the mechanism explained in this paper. However, in this scenario the screening mechanism originates from states in two different bands, rather than from a single band in which the extent of layer polarization evolves with momentum, as in the case of TDBG.

The self-consistently determined layer-potential framework may also be applied to scanning tunneling microscopy (STM) measurements versus gate bias, which corresponds to tracing a diagonal line in the displacement field and filling factor plane (effectively setting the density of carriers in the top gate to zero). The differing electrostatics between singly and doubly gated multilayer devices may help clarify the recent distinctions in symmetry-breaking regimes observed between transport and STM devices [51,52].

Other flat-band moiré systems, such as twisted bilayer $MoTe_2$ [53,54] and twisted bilayer WSe_2 [55,56], also exhibit gate-tracking behavior in certain regions of their carrier density and displacement field parameter space. While these systems lack the internal AB stacking, by construction the low-energy theory of bilayer systems of twisted bilayer $MoTe_2$ and twisted bilayer WSe_2 is constructed from two surface pockets present in each layer. As such, our theory is likely able to capture similar effects in those systems, along with many other van der Waals multilayer structures.

Before concluding, we would like to clarify the claims of our manuscript in relation to the existing body of literature. Experimentally local high resistance features, as those shown in Fig. 1(a) for $\nu < 0$, have been reported in literature in the past, e.g., Refs. [22–30,32,33,57–60], and referred to as resistance "streaks" or "resistance ridges." Generally, these features can occur for several reasons, as some authors theoretically explain [57–60]; however, our analysis explains why some of these resistance features as well as symmetry-breaking boundaries tend to track a single-gate voltage. A unifying mechanism for such single-gate tracking, which forms the key result of our manuscript, to our knowledge, has not been discussed in the literature although the question of electrostatic screening due to gates in graphene systems [37,39,40], and even twisted double-bilayer graphene in particular [61], has been discussed in the past.

ACKNOWLEDGMENTS

We thank Felix von Oppen, Chunli Huang, Vo Tien Phong, and Étienne Lantagne-Hurtubise for useful discussions. We would also like to thank the HPC Service of Zentraleinrichtung für Datenverarbeitung, Freie Universität Berlin for computing time. K.K. was supported by Deutsche Forschungsgemeinschaft through CRC 183 (Project No. C02), by a joint ANR-DFG project (TWISTGRAPH Grant No. ANR-21-CE47-0018), and by a grant from the Simons Foundation (Grant No. SFI-MPS-NFS-00006741-12, P.T.) in the Simons Collaboration on New Frontiers in Superconductivity. D.W. was supported by an appointment to the Intelligence Community Postdoctoral Research Fellowship Program at University of Washington administered by Oak Ridge Institute for Science and Education through an interagency agreement between the U.S. Department of Energy and the Office of the Director of National Intelligence. J.F. acknowledges support from the European Research Council under the European Union Horizon 2020 Research and Innovation Programme under Grant No. 951541, the Natural Sciences and Engineering Research Council of Canada, the Canadian Institute for Advanced Research, the Max Planck - University of British Columbia - University of Tokyo Centre for Quantum Materials, and the Canada First Research Excellence Fund Quantum Materials and Future Technologies Program. M.Y. acknowledges support from National Science Foundation CAREER Grant No. DMR-2041972 and the U.S. Department of Energy, Basic Energy Science Programs under Grant No. DE-SC0023062. C.L. was supported by start-up funds from Florida State University and the National High Magnetic Field Laboratory. The National High Magnetic Field Laboratory is supported by the National Science Foundation through Grant No. NSF/DMR-2128556 and the State of Florida.

DATA AVAILABILITY

The data that support the findings of this article are openly available [62].

[1] Y. Cao, V. Fatemi, A. Demir, S. Fang, S. L. Tomarken, J. Y. Luo, J. D. Sanchez-Yamagishi, K. Watanabe, T. Taniguchi, E. Kaxiras, R. C. Ashoori, and P. Jarillo-Herrero, Correlated insulator behaviour at half-filling in magic-angle graphene superlattices, Nature (London) **556**, 80 (2018).

[2] Y. Cao, V. Fatemi, S. Fang, K. Watanabe, T. Taniguchi, E. Kaxiras, and P. Jarillo-Herrero, Unconventional superconductivity in magic-angle graphene superlattices, Nature (London) **556**, 43 (2018).

[3] M. Yankowitz, S. Chen, H. Polshyn, Y. Zhang, K. Watanabe, T. Taniguchi, D. Graf, A. F. Young, and C. R. Dean, Tuning superconductivity in twisted bilayer graphene, Science **363**, 1059 (2019).

[4] Z. Hao, A. M. Zimmerman, P. Ledwith, E. Khalaf, D. H. Najafabadi, K. Watanabe, T. Taniguchi, A. Vishwanath, and P. Kim, Electric field–tunable superconductivity in alternating-twist magic-angle trilayer graphene, Science **371**, 1133 (2021).

[5] M. Oh, K. P. Nuckolls, D. Wong, R. L. Lee, X. Liu, K. Watanabe, T. Taniguchi, and A. Yazdani, Evidence for unconventional superconductivity in twisted bilayer graphene, Nature (London) **600**, 240 (2021).

[6] X. Lu, P. Stepanov, W. Yang, M. Xie, M. A. Aamir, I. Das, C. Urgell, K. Watanabe, T. Taniguchi, G. Zhang, A. Bachtold, A. H. MacDonald, and D. K. Efetov, Superconductors, orbital magnets and correlated states in magic-angle bilayer graphene, Nature (London) **574**, 653 (2019).

[7] Y. Cao, D. Rodan-Legrain, J. M. Park, N. F. Q. Yuan, K. Watanabe, T. Taniguchi, R. M. Fernandes, L. Fu, and P. Jarillo-Herrero, Nematicity and competing orders in superconducting magic-angle graphene, Science **372**, 264 (2021).

[8] X. Liu, Z. Wang, K. Watanabe, T. Taniguchi, O. Vafek, and J. I. A. Li, Tuning electron correlation in magic-angle twisted bilayer graphene using Coulomb screening, Science **371**, 1261 (2021).

[9] H. S. Arora, R. Polski, Y. Zhang, A. Thomson, Y. Choi, H. Kim, Z. Lin, I. Z. Wilson, X. Xu, J.-H. Chu, K. Watanabe, T. Taniguchi, J. Alicea, and S. Nadj-Perge, Superconductivity in metallic twisted bilayer graphene stabilized by WSe_2, Nature (London) **583**, 379 (2020).

[10] P. Stepanov, I. Das, X. Lu, A. Fahimniya, K. Watanabe, T. Taniguchi, F. H. L. Koppens, J. Lischner, L. Levitov, and D. K. Efetov, Untying the insulating and superconducting orders in magic-angle graphene, Nature (London) **583**, 375 (2020).

[11] Y. Saito, J. Ge, K. Watanabe, T. Taniguchi, and A. F. Young, Independent superconductors and correlated insulators in twisted bilayer graphene, Nat. Phys. **16**, 926 (2020).

[12] J. Cai, E. Anderson, C. Wang, X. Zhang, X. Liu, W. Holtzmann, Y. Zhang, F. Fan, T. Taniguchi, K. Watanabe, Y. Ran, T. Cao, L. Fu, D. Xiao, W. Yao, and X. Xu, Signatures of fractional quantum anomalous Hall states in twisted $MoTe_2$, Nature (London) **622**, 63 (2023).

[13] H. Park, J. Cai, E. Anderson, Y. Zhang, J. Zhu, X. Liu, C. Wang, W. Holtzmann, C. Hu, Z. Liu, T. Taniguchi, K. Watanabe, J.-H. Chu, T. Cao, L. Fu, W. Yao, C.-Z. Chang, D. Cobden, D. Xiao, and X. Xu, Observation of fractionally quantized anomalous Hall effect, Nature (London) **622**, 74 (2023).

[14] Y. Zeng, Z. Xia, K. Kang, J. Zhu, P. Knüppel, C. Vaswani, K. Watanabe, T. Taniguchi, K. F. Mak, and J. Shan, Thermodynamic evidence of fractional Chern insulator in moiré $MoTe_2$, Nature (London) **622**, 69 (2023).

[15] F. Xu, Z. Sun, T. Jia, C. Liu, C. Xu, C. Li, Y. Gu, K. Watanabe, T. Taniguchi, B. Tong, J. Jia, Z. Shi, S. Jiang, Y. Zhang, X. Liu, and T. Li, Observation of integer and fractional quantum anomalous Hall effects in twisted bilayer $MoTe_2$, Phys. Rev. X **13**, 031037 (2023).

[16] B. A. Foutty, C. R. Kometter, T. Devakul, A. P. Reddy, K. Watanabe, T. Taniguchi, L. Fu, and B. E. Feldman, Mapping twist-tuned multiband topology in bilayer WSe_2, Science **384**, 343 (2024).

[17] H. Zhou, L. Holleis, Y. Saito, L. Cohen, W. Huynh, C. L. Patterson, F. Yang, T. Taniguchi, K. Watanabe, and A. F. Young, Isospin magnetism and spin-polarized superconductivity in Bernal bilayer graphene, Science **375**, 774 (2022).

[18] H. Zhou, T. Xie, A. Ghazaryan, T. Holder, J. R. Ehrets, E. M. Spanton, T. Taniguchi, K. Watanabe, E. Berg, M. Serbyn, and A. F. Young, Half- and quarter-metals in rhombohedral trilayer graphene, Nature (London) **598**, 429 (2021).

[19] S. C. de la Barrera, S. Aronson, Z. Zheng, K. Watanabe, T. Taniguchi, Q. Ma, P. Jarillo-Herrero, and R. Ashoori, Cascade of isospin phase transitions in Bernal-stacked bilayer graphene at zero magnetic field, Nat. Phys. **18**, 771 (2022).

[20] Y. Zhang, R. Polski, A. Thomson, Étienne Lantagne-Hurtubise, C. Lewandowski, H. Zhou, K. Watanabe, T. Taniguchi, J. Alicea, and S. Nadj-Perge, Enhanced superconductivity in spin-orbit proximitized bilayer graphene, Nature (London) **613**, 268 (2023).

[21] H. Zhou, T. Xie, T. Taniguchi, K. Watanabe, and A. F. Young, Superconductivity in rhombohedral trilayer graphene, Nature (London) **598**, 434 (2021).

[22] Z. Lu, T. Han, Y. Yao, A. P. Reddy, J. Yang, J. Seo, K. Watanabe, T. Taniguchi, L. Fu, and L. Ju, Fractional quantum anomalous Hall effect in multilayer graphene, Nature (London) **626**, 759 (2024).

[23] Z. Lu, T. Han, Y. Yao, Z. Hadjri, J. Yang, J. Seo, L. Shi, S. Ye, K. Watanabe, T. Taniguchi, and L. Ju, Extended quantum anomalous Hall states in graphene/hBN moiré superlattices, Nature (London) **637**, 1090 (2025).

[24] D. Waters, A. Okounkova, R. Su, B. Zhou, J. Yao, K. Watanabe, T. Taniguchi, X. Xu, Y.-H. Zhang, J. Folk, and M. Yankowitz, Chern insulators at integer and fractional filling in moiré pentalayer graphene, Phys. Rev. X **15**, 011045 (2025).

[25] X. Liu, Z. Hao, E. Khalaf, J. Y. Lee, Y. Ronen, H. Yoo, D. Haei Najafabadi, K. Watanabe, T. Taniguchi, A. Vishwanath, and P. Kim, Tunable spin-polarized correlated states in twisted double bilayer graphene, Nature (London) **583**, 221 (2020).

[26] M. Kuiri, C. Coleman, Z. Gao, A. Vishnuradhan, K. Watanabe, T. Taniguchi, J. Zhu, A. H. MacDonald, and J. Folk, Spontaneous time-reversal symmetry breaking in twisted double bilayer graphene, Nat. Commun. **13**, 6468 (2022).

[27] Y. Cao, D. Rodan-Legrain, O. Rubies-Bigorda, J. M. Park, K. Watanabe, T. Taniguchi, and P. Jarillo-Herrero, Tunable correlated states and spin-polarized phases in twisted bilayer-bilayer graphene, Nature (London) **583**, 215 (2020).

[28] D. Waters, R. Su, E. Thompson, A. Okounkova, E. Arreguin-Martinez, M. He, K. Hinds, K. Watanabe, T. Taniguchi, X. Xu, Y.-H. Zhang, J. Folk, and M. Yankowitz, Topological flat bands in a family of multilayer graphene moiré lattices, Nat. Commun. **15**, 10552 (2024).

[29] M. He, Y. Li, J. Cai, Y. Liu, K. Watanabe, T. Taniguchi, X. Xu, and M. Yankowitz, Symmetry breaking in twisted double bilayer graphene, Nat. Phys. **17**, 26 (2021).

[30] G. W. Burg, J. Zhu, T. Taniguchi, K. Watanabe, A. H. MacDonald, and E. Tutuc, Correlated insulating states in twisted double bilayer graphene, Phys. Rev. Lett. **123**, 197702 (2019).

[31] H. Polshyn, Y. Zhang, M. A. Kumar, T. Soejima, P. Ledwith, K. Watanabe, T. Taniguchi, A. Vishwanath, M. P. Zaletel, and A. F. Young, Topological charge density waves at half-integer filling of a moiré superlattice, Nat. Phys. **18**, 42 (2022).

[32] R. Su, D. Waters, B. Zhou, K. Watanabe, T. Taniguchi, Y.-H. Zhang, M. Yankowitz, and J. Folk, Moiré-driven topological electronic crystals in twisted graphene, Nature (London) **637**, 1084 (2025).

[33] S. Xu, M. M. Al Ezzi, N. Balakrishnan, A. Garcia-Ruiz, B. Tsim, C. Mullan, J. Barrier, N. Xin, B. A. Piot, T. Taniguchi, K. Watanabe, A. Carvalho, A. Mishchenko, A. K. Geim, V. I. Fal'ko, S. Adam, A. H. C. Neto, K. S. Novoselov, and Y. Shi,

Tunable Van Hove singularities and correlated states in twisted monolayer–bilayer graphene, Nat. Phys. **17**, 619 (2021).

[34] See Supplemental Material at http://link.aps.org/supplemental/10.1103/j1zf-v3j5 for further details, which includes Refs. [63–66].

[35] E. McCann and V. I. Fal'ko, Landau-level degeneracy and quantum Hall effect in a graphite bilayer, Phys. Rev. Lett. **96**, 086805 (2006).

[36] J. Nilsson, A. H. Castro Neto, F. Guinea, and N. M. R. Peres, Electronic properties of bilayer and multilayer graphene, Phys. Rev. B **78**, 045405 (2008).

[37] E. McCann and M. Koshino, The electronic properties of bilayer graphene, Rep. Prog. Phys. **76**, 056503 (2013).

[38] K. Kolář, Y. Zhang, S. Nadj-Perge, F. von Oppen, and C. Lewandowski, Electrostatic fate of *n*-layer moiré graphene, Phys. Rev. B **108**, 195148 (2023).

[39] M. Koshino, Interlayer screening effect in graphene multilayers with *ABA* and *ABC* stacking, Phys. Rev. B **81**, 125304 (2010).

[40] M. Koshino and E. McCann, Gate-induced interlayer asymmetry in *ABA*-stacked trilayer graphene, Phys. Rev. B **79**, 125443 (2009).

[41] F. Guinea, Charge distribution and screening in layered graphene systems, Phys. Rev. B **75**, 235433 (2007).

[42] $H_\perp$ can also be obtained by considering the standard density-density interaction and incorporating the layer dependence of the Coulomb interaction. In that viewpoint, the $H_\perp$ terms arise from the $q = 0$ Hartree contribution of charges localized in different layers [38]. To build qualitative intuition for $H_\perp$, however, we focus here on Eq. (4) for the layer potentials U_l.

[43] Physically, this relation between W_l and $\partial\mu/\partial U_l$ can be understood by realizing that the total chemical potential shifts due to the layer potentials with the amount of each shift set by the relative density of charges at the Fermi level on that layer.

[44] Y. Shi, S. Xu, Y. Yang, S. Slizovskiy, S. V. Morozov, S.-K. Son, S. Ozdemir, C. Mullan, J. Barrier, J. Yin, A. I. Berdyugin, B. A. Piot, T. Taniguchi, K. Watanabe, V. I. Fal'ko, K. S. Novoselov, A. K. Geim, and A. Mishchenko, Electronic phase separation in multilayer rhombohedral graphite, Nature (London) **584**, 210 (2020).

[45] Y. Guo, O. I. Sheekey, T. Arp, K. Kolář, T. Charpentier, L. Holleis, B. Foutty, A. Keough, M. Kang-Chou, M. E. Huber, T. Taniguchi, K. Watanabe, C. Lewandowski, and A. F. Young, Flat band surface state superconductivity in thick rhombohedral graphene, arXiv:2511.17423.

[46] M. Kumar, D. Waleffe, A. Okounkova, R. Tejani, K. Watanabe, T. Taniguchi, Étienne Lantagne-Hurtubise, J. Folk, and M. Yankowitz, Pervasive spin-triplet superconductivity in rhombohedral graphene, arXiv:2511.16578.

[47] J. Deng, J. Xie, H. Li, T. Taniguchi, K. Watanabe, J. Shan, K. F. Mak, and X. Liu, Superconductivity and ferroelectric orbital magnetism in semimetallic rhombohedral hexalayer graphene, arXiv:2508.15909.

[48] M. Kumar, D. Waleffe, A. Okounkova, R. Tejani, V. Tien Phong, K. Watanabe, T. Taniguchi, C. Lewandowski, J. Folk, and M. Yankowitz, Superconductivity from dual-surface carriers in rhombohedral graphene, arXiv:2507.18598.

[49] The regime of $\alpha < 0$ occurs when $\rho e^2 \Delta d/\tilde{\varepsilon}_\perp \varepsilon_0 \gg 1$. By comparison the Stoner criterion takes the form $\rho \frac{e^2}{\tilde{\varepsilon}\varepsilon_0 k_F} = 1$, where k_F is the Fermi momentum and $\tilde{\varepsilon} \simeq \tilde{\varepsilon}_\perp$ is the relevant (likely in-plane) dielectric constant. Generically, $1/k_F \gtrsim \Delta d$ as average interparticle separation exceeds the layer spacing. As such, the Stoner criterion will typically be satisfied before $\rho e^2 \Delta d/\tilde{\varepsilon}_\perp \varepsilon_0 \gg 1$. The system will then prefer to undergo symmetry breaking and reduce α.

[50] U. Zondiner, A. Rozen, D. Rodan-Legrain, Y. Cao, R. Queiroz, T. Taniguchi, K. Watanabe, Y. Oreg, F. von Oppen, A. Stern, E. Berg, P. Jarillo-Herrero, and S. Ilani, Cascade of phase transitions and Dirac revivals in magic-angle graphene, Nature (London) **582**, 203 (2020).

[51] Y. Liu, A. Gupta, Y. Choi, Y. Vituri, H. Stoyanov, J. Xiao, Y. Wang, H. Zhou, B. Barick, T. Taniguchi, K. Watanabe, B. Yan, E. Berg, A. F. Young, H. Beidenkopf, and N. Avraham, Visualizing incommensurate inter-valley coherent states in rhombohedral trilayer graphene, arXiv:2411.11163.

[52] W.-Y. Liao, W.-X. Wang, S. Zhang, Y. Zhang, L.-H. Tong, W. Zhang, H. Cai, Y. Tian, Y. Hu, L. Zhang, L. Zhang, Z. Qin, and L.-J. Yin, Intervalley coherent order in rhombohedral tetralayer graphene on MoS_2, Phys. Rev. Lett. **135**, 046202 (2025).

[53] H. Park, J. Cai, E. Anderson, X.-W. Zhang, X. Liu, W. Holtzmann, W. Li, C. Wang, C. Hu, Y. Zhao, T. Taniguchi, K. Watanabe, J. Yang, D. Cobden, J.-H. Chu, N. Regnault, B. Andrei Bernevig, L. Fu, T. Cao, D. Xiao, *et al.*, Ferromagnetism and topology of the higher flat band in a fractional Chern insulator, Nat. Phys. **21**, 549 (2025).

[54] F. Xu, X. Chang, J. Xiao, Y. Zhang, F. Liu, Z. Sun, N. Mao, N. Peshcherenko, J. Li, K. Watanabe, T. Taniguchi, B. Tong, L. Lu, J. Jia, D. Qian, Z. Shi, Y. Zhang, X. Liu, S. Jiang, and T. Li, Interplay between topology and correlations in the second moiré band of twisted bilayer $MoTe_2$, Nat. Phys. **21**, 542 (2025).

[55] Y. Xia, Z. Han, K. Watanabe, T. Taniguchi, J. Shan, and K. F. Mak, Superconductivity in twisted bilayer WSe_2, Nature (London) **637**, 833 (2024).

[56] Y. Guo, J. Pack, J. Swann, L. Holtzman, M. Cothrine, K. Watanabe, T. Taniguchi, D. G. Mandrus, K. Barmak, J. Hone, A. J. Millis, A. Pasupathy, and C. R. Dean, Superconductivity in 5.0° twisted bilayer WSe_2, Nature (London) **637**, 839 (2025).

[57] R. Yagi, T. Hirahara, R. Ebisuoka, T. Nakasuga, S. Tajima, K. Watanabe, and T. Taniguchi, Low-energy band structure and even-odd layer number effect in AB-stacked multilayer graphene, Sci. Rep. **8**, 13018 (2018).

[58] Y. Shi, S. Che, K. Zhou, S. Ge, Z. Pi, T. Espiritu, T. Taniguchi, K. Watanabe, Y. Barlas, R. Lake, and C. N. Lau, Tunable Lifshitz transitions and multiband transport in tetralayer graphene, Phys. Rev. Lett. **120**, 096802 (2018).

[59] F. Mukai, K. Horii, R. Ebisuoka, K. Watanabe, T. Taniguchi, and R. Yagi, Unconventional satellite resistance peaks in moiré superlattice of *h*-BN/ AB-stacked tetralayer-graphene heterostructures, Commun. Phys. **4**, 109 (2021).

[60] T. Hirahara, R. Ebisuoka, T. Oka, T. Nakasuga, S. Tajima, K. Watanabe, T. Taniguchi, and R. Yagi, Multilayer graphene shows intrinsic resistance peaks in the carrier density dependence, Sci. Rep. **8**, 13992 (2018).

[61] F. Mukai, K. Horii, N. Hata, R. Ebisuoka, K. Watanabe, T. Taniguchi, and R. Yagi, On dielectric screening in twisted double bilayer graphene, J. Phys. Soc. Jpn. **90**, 124702 (2021).

[62] K. Kolar, D. Waters, J. Folk, M. Yankowitz, and C. Lewandowski, Dataset for single-gate tracking behavior in flat-band multilayer graphene devices, Zenodo, 2025, https://doi.org/10.5281/zenodo.17708316.

[63] J. Herzog-Arbeitman, Y. Wang, J. Liu, P. M. Tam, Z. Qi, Y. Jia, D. K. Efetov, O. Vafek, N. Regnault, H. Weng, Q. Wu, B. Andrei Bernevig, and J. Yu, Moiré fractional Chern insulators II: First-principles calculations and continuum models of rhombohedral graphene superlattices, Phys. Rev. B **109**, 205122 (2024).

[64] R. Bistritzer and A. H. MacDonald, Moire bands in twisted double-layer graphene, Proc. Natl. Acad. Sci. USA **108**, 12233 (2011).

[65] Y. H. Kwan, J. Yu, J. Herzog-Arbeitman, D. K. Efetov, N. Regnault, and B. Andrei Bernevig, Moiré fractional Chern insulators III: Hartree-Fock phase diagram, magic angle regime for Chern insulator states, the role of the moiré potential and Goldstone gaps in rhombohedral graphene superlattices, Phys. Rev. B **112**, 075109 (2025).

[66] E. Cancès and C. Le Bris, Can we outperform the DIIS approach for electronic structure calculations? Int. J. Quantum Chem. **79**, 82 (2000).